Volume 10
Number 39
21 October 2022
Pages 14353–14780

Journal of Materials Chemistry C

Materials for optical, magnetic and electronic devices

rsc.li/materials-c

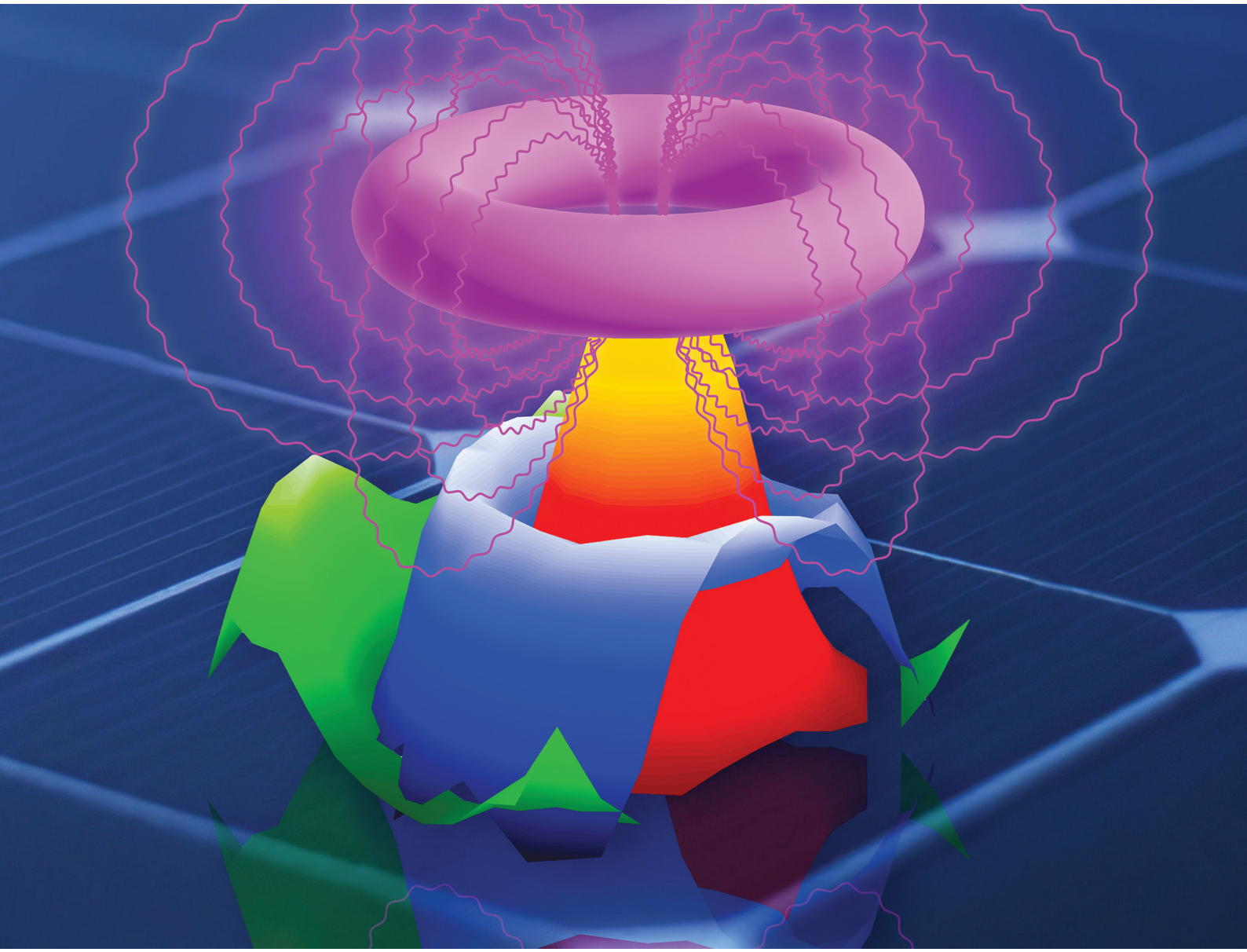

ISSN 2050-7526

ROYAL SOCIETY OF CHEMISTRY

PAPER

Eugen Stamate *et al.*

Preferential zinc sputtering during the growth of aluminum doped zinc oxide thin films by radio frequency magnetron sputtering

Journal of Materials Chemistry C

ROYAL SOCIETY OF CHEMISTRY

PAPER

View Article Online
View Journal | View Issue

Check for updates

Cite this: J. Mater. Chem. C, 2022, 10, 14444

Preferential zinc sputtering during the growth of aluminum doped zinc oxide thin films by radio frequency magnetron sputtering†

Kion Norrman,[ab] Poul Norby [a] and Eugen Stamate *[c]

Received 25th May 2022,
Accepted 15th August 2022

DOI: 10.1039/d2tc02180c

rsc.li/materials-c

Aluminum doped ZnO is one of the main candidates to replace indium tin oxide used as a transparent conducting oxide. Despite the intensive research, the mechanism behind the poor thin-film-resistivity uniformity over the sample deposited by magnetron sputtering is not completely understood. Several independent reports correlate the mirroring of an erosion track on the substrate with energetic negative oxygen ions. However, their role on assisting the thin film growth is not known. In this work, the physical and chemical properties of aluminum doped ZnO are measured with a high spatial resolution at different thin film deposition pressures. The results show that Zn depletion by energetic negative oxygen ion re-sputtering is the main factor correlating with the resistivity and the band gap energy profiles of the deposited films.

1. Introduction

Transparent conducting oxides (TCOs) are essential thin films for solar cells, touch panels, organic light emitting diodes and smart windows.[1–3] Recent applications also include plasmonics,[4] electron transport layers,[5] gas sensors[6] and optical spacers.[7] This large market comes with high demands for the fabrication cost, throughput, and availability of raw materials. So far, indium tin oxide (ITO) deposited by magnetron sputtering provides a resistivity below 2×10^{-4} Ω cm and an average transmittance of above 80%, which makes it the most used TCO.[1] However, the limited availability of indium, coupled with its intensive use, requires a timely replacement. ZnO is an n-type semiconductor that can reach resistivities below 10^{-3} Ω cm by doping with several elements, among which Al is regarded as a very promising dopant being one of the most abundant metals. While aluminum doped zinc oxide (AZO) with resistivities below 1×10^{-3} Ω cm has been reported by several research groups,[8–21] the main problem stands on the limited area (smaller than the sputtering target) were such vales have been measured, which most of the times is near the edge of the substrate. A schematic cross section of a circular magnetron sputtering head is shown in Fig. 1(a) including the set of permanent magnets placed behind the target, the high-density plasma of a torus shape, and the substrate facing the target in a parallel configuration. The magnetic field increases the collision probability of electrons with the neutral gas, elevating considerably the plasma density, with a direct impact on the sputtering rate. This particular geometry results in a very well-defined erosion track on the target surface, which is adjacent to the high-density plasma torus. AZO targets are conductive enough to sustain direct current (DC), pulsed DC, medium-frequency, radio-frequency (RF), or high-power impulse operation modes.[22] Electrons and ions form a quasi-neural plasma in the space between the negatively biased target (cathode) and the ground (anode) except for the cathode, anode and substrate sheaths. The cathode sheath thickness and the voltage-drop across it, with respect to plasma potential, depend on the operation mode, besides the other main parameters such as the plasma density and target material.[22] The anode sheath is also influenced by various factors, including the magnetron configuration, operation mode, proximity to targets and surface conditions. A sheath can also form in front of the substrate depending on its bias. The needed oxygen can be embedded in the target (oxide target) or supplied in the gas phase for metallic targets (reactive sputtering). Despite a lower cost for metallic targets, the complex control of the reactive process and contamination issues associated with Zn favors AZO deposition from oxide targets.[2] DC and RF operation modes are essentially different when taking into account the discharge mechanism.[9,22] However, in both cases, the high flux of positive ions impinging on

[a] Department of Energy Conversion and Storage, Technical University of Denmark, Anker Engelunds Vej, Kgs. Lyngby 2800, Denmark
[b] Center for Integrative Petroleum Research, College of Petroleum Engineering & Geosciences, King Fahd University of Petroleum and Minerals, KFUPM Box 5070, 34464 Dhahran, Saudi Arabia
[c] National Centre for Nano Fabrication and Characterization, Technical University of Denmark, Ørsteds Plads, Kgs. Lyngby 2800, Denmark. E-mail: eust@dtu.dk

† Electronic supplementary information (ESI) available: [DETAILS]. See DOI: https://doi.org/10.1039/d2tc02180c

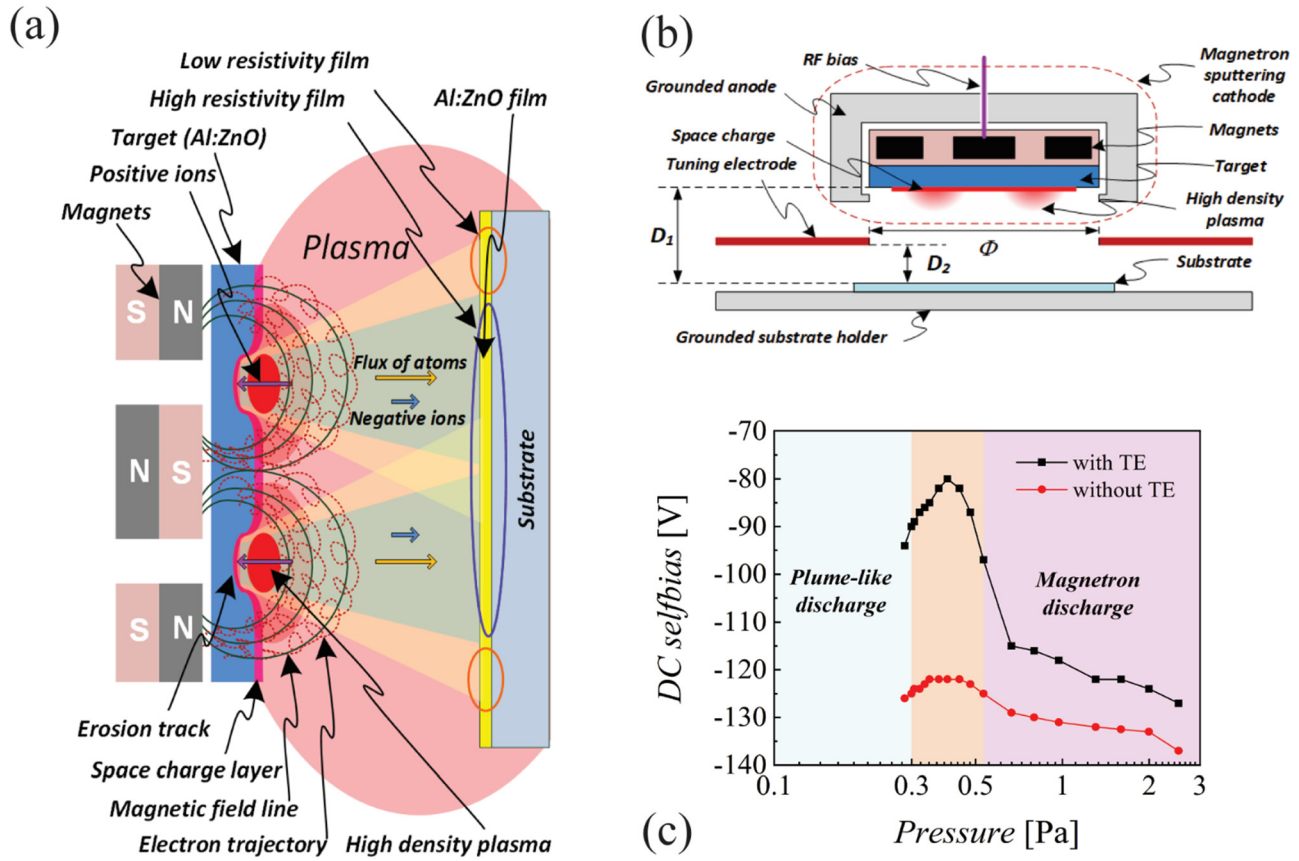

Fig. 1 (a) Schematic cross section of a circular magnetron sputtering head. (b) Geometric details on the target, tuning-electrode and substrate arrangement. (c) Typical DC self-bias dependence on pressures with and without the tuning-electrode measured with an AZO target for 30 W RF power.

the target at the erosion track releases low-energy secondary electrons that can easily form negative oxygen ions (by electron attachment) to be then accelerated towards the substrate by the cathode sheath.[23–25] The correlation between the spatial distribution of the resistivity with the erosion track on the target surface was reported more than three decades ago and is believed to be attributed to two main factors: 1) the role of energetic negative oxygen ions[9] and 2) atomic oxygen.[3] The first assumption was verified rather recently by Bikowski *et al.*[26] Moreover, it was also reported that the negative oxygen ions reach higher energies in DC than those in RF at 13.56 MHz with a trend of further decreasing energies by RF excitation at even higher frequencies such as 27.12 MHz.[26] As far as it is known, there is yet no direct evidence correlating the resistivity with atomic oxygen. Metal oxide thin films deposited by magnetron sputtering are widely used in various applications including thin film transistors, energy devices and sensors where uniformity is a critical parameter.[27,28] This underlines the importance to know the role of negative oxygen ions during the thin film growth of metal oxides. This issue was reviewed by Ellmer *et al.* including several options to diminish the influence of negative ions.[29] When depositing AZO by DC magnetron sputtering using Ar, Kr, and Xe, Sato *et al.* attributed the enhanced degradation observed for Kr and Xe with possible preferential Zn re-sputtering.[30] However, Ar is the preferred choice for TCO deposition. In two very recent publications, Stamate reported AZO resistivity variations larger than two orders of magnitude for a span on the substrate of less than 10 mm[31] and demonstrated the possibility to reduce the detrimental role of negative ions by reducing their energy with a tuning electrode (TE)[32] as schematically presented in Fig. 1(b). Moreover, the spatial distribution of plasma parameters resolved with a dual, electrostatic-thermal probe revealed no direct correlation between the erosion track and plasma density, electron temperature and plasma potential.[33] Stamate found it of high relevance that the narrow range of a low DC self-bias that ensures a minimum energy for negative ions corresponds to a transition region from a plume-like plasma discharge to the normal magnetron sputtering operation as presented in Fig. 1(c) where the DC self-bias as function of pressure is presented with and without the TE.[32,33] Very recently, it was demonstrated that gallium doped zinc oxide and ITO exhibit the same dependence of the self-bias with pressures as reported for AZO; however, only AZO exhibited the most noticeable correlation of the optoelectronic properties with the erosion track.[34] The optoelectronic and analytical properties of AZO thin films by sputtering have been intensively studied by X-ray photoelectron spectroscopy (XPS),[35–38] X-ray diffraction (XRD)[35,38–41] and Raman spectroscopy[36,39] for various parameters (*e.g.*, pressure,[42–44] power,[45–47] target to substrate distance,[31,48] substrate material,[49] oxygen gas fraction,[50,51]

substrate temperature,[38] plasma excitation mode,[18,52,53] annealing temperature,[54,55] target erosion,[16] and Al doping fraction[56]). However, so far, no conclusive correlation has been reported between the role of negative oxygen ions and the physical and chemical properties of AZO thin films as to be able to obtain resistivities below 10^{-3} Ω cm for a deposited area comparable with that of the target. This work presents the spatially resolved physical and chemical parameters of AZO thin films deposited by radio-frequency magnetron sputtering using an oxide target with the aim of understanding the link between the intrinsic particularities of the magnetron sputtering discharge and the AZO thin film properties.

2. Experimental section

Materials

The AZO sputtering target (2 inch in diameter, 2% Al_2O_3 to 98% ZnO by weight) was supplied by Kurt Lesker (Jefferson Hills, USA). The AZO thin films were deposited on 10 × 50 mm^2 soda lime glass substrates (0.5 mm in thickness) cut from 100 × 100 mm^2 plates provided by Semiconductor Wafer, Inc. (Hsinchu, Taiwan). Up to 8 samples were placed on a large substrate holder that allowed the rotation exposure to the cathode, without breaking the vacuum or turning off the plasma discharge. A certain positioning of the large plate accommodating the TE was used as a shutter during the time needed for the small adjustments of the deposition parameters.[34] All samples were deposited at a 30 W RF power for 30 min. There was no intentional heating of the substrate except for the mild effect of plasma exposure (below 50 °C).

Thin film deposition

The AZO target was mounted using a TORUS® magnetron sputtering cathode (Kurt Lesker, Jefferson Hills, USA) with a balanced magnetic field configuration. Following prior optimization, the target-to-substrate distance (see D_1 in Fig. 1(b)) was kept at 35 mm and the tuning-electrode-to-substrate distance (see D_2 in Fig. 1(b)) was kept at 10 mm, for a TE opening, Φ = 60 mm.

Opto-electronic characterization

The sheet resistance was measured using a custom-made system and a commercial system (KSR-4, Everbeing Int'l Corp., Hsinchu, Taiwan). The custom-made system consisted of two pads distributed perpendicular to the sample length for providing a uniform current and two pins for measuring the drop voltage. The film thickness was measured using a Filmetrics 20 instrument (KLA Co, San Diego, USA). The transmittance spectra were recorded using a Cary 100 UV-VIS spectrometer from Agilent (Victoria, Australia).

TOF-SIMS

A TOF-SIMS IV (ION-TOF GmbH, Münster, Germany) was employed to analyze the samples. 25 ns Pulses of 25 keV Bi^+ (primary ions) were arranged to form ion packets with a nominal temporal extent of <0.9 ns at a repetition rate of 10 kHz, yielding a target current of 0.8 pA. These primary ion conditions were used to obtain ion images on 50 × 6 mm^2 surface areas (512 × 64 pixels, 1 scan). For all analyses, the electron bombardment (20 eV) was used to minimize the charge build-up at the surface. Desorbed secondary ions were accelerated to 2 keV, mass analyzed in the flight tube, and post-accelerated to 10 keV before detection. The line profiles were extracted from the ion images.

XPS

An ESCALAB XI^+ X-ray photoelectron spectrometer microprobe (Thermo Fisher Scientific, East Grinstead, UK) was employed to analyze the samples. A monochromatic Al-Kα X-ray source with a 650 μm spot size and a take-off angle of 90° from the surface plane was used. Atomic concentrations were determined from survey spectra (0–1300 eV, 100 eV detector pass energy, 1 eV step size, 50 ms dwell time, and 2 scans) and were calculated by determining the relevant integral peak intensities using a Smart type background. High-resolution Zn-$2p_{3/2}$ and O-1s spectra were recorded (25 eV detector pass energy, 0.1 eV step size, 50 ms dwell time, and 2 scans) and the Thermo Fisher Scientific Avantage software (version 5.979, build 06465) was employed for peak fitting, using a Smart type background, a full width at half maximum (FWHM) of 1.5 eV, and a Gauss/Lorentz mix value of 70%. A spectrum was acquired each 0.5 mm along the entire sample corresponding to 100 surface locations.

XRD

Crystallographic mapping of the orientation of the deposited AZO layer was performed by X-ray diffraction using a Rigaku SmartLab diffractometer in the Bragg–Brentano configuration (Cu–Kα radiation). Using a *x*/*y* translation stage, the 50 × 50 mm^2 AZO samples were mapped with a resolution of 4 × 4 mm^2 using a 5 × 5 mm^2 beam size controlled by a motorized divergence slit on the incoming X-ray beam. The 100, 200 and 110 reflections were fitted using a Pseudo Voigt function, determining the position, intensity and FWHM of the reflections. The 2D crystal structure analysis of the AZO thin films was performed *via* X-ray diffraction (Tokyo, Japan), Bragg–Brentano geometry, Cu–Kα radiation, 10–90° in 2θ and 0.02 step size degrees.

3. Results and discussion

The spatial distributions of the sheet resistance, film thickness and resistivity measured on 10 × 50 mm^2 substrates at different pressures are shown in Fig. 2(a–c), respectively. This type of variation has been presented and discussed very recently and can be summarized as follows.[31–33] The discharge is in the plume-like mode at 0.27 Pa with a difference of almost two orders of magnitude between the sheet resistance values at $r = 0$ and $|r| \cong 17$ mm and a high re-sputtering rate for $|r| < 10$ mm (see the reduced thin film thickness). By reducing the target-to-substrate distance or increasing the RF discharge power, the

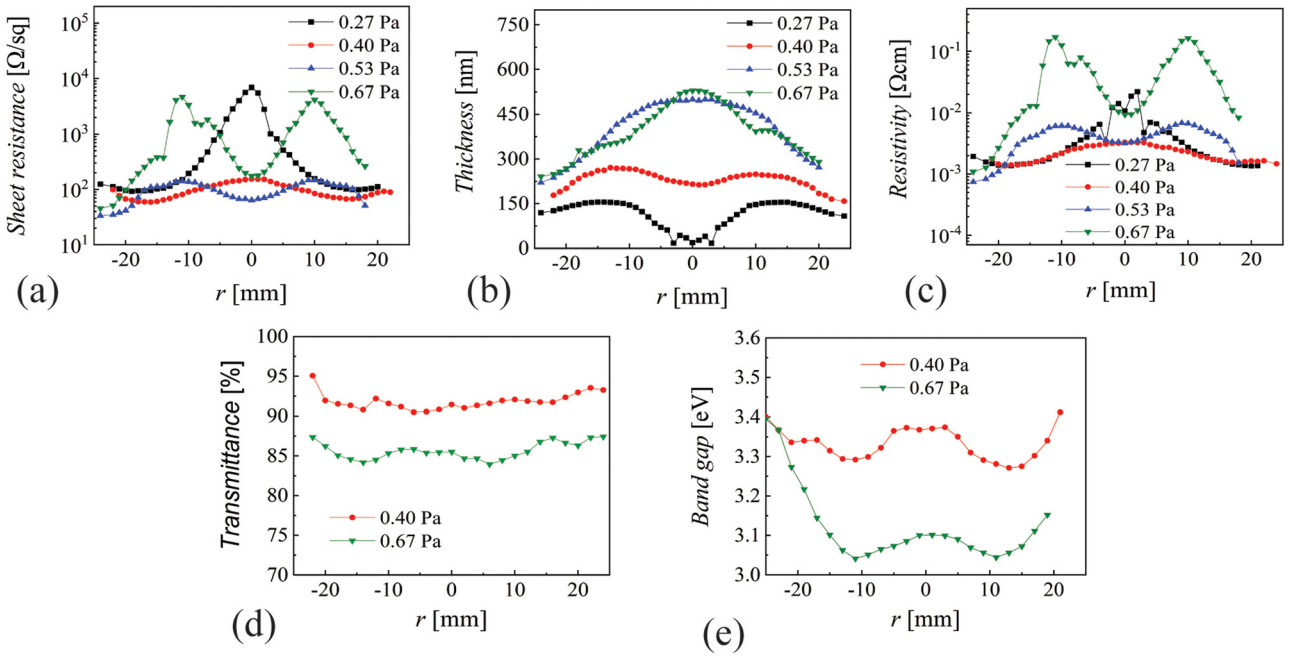

Fig. 2 Spatial distributions of the (a) sheet resistance, (b) film thickness, (c) resistivity, (d) average transmittance and (e) band gap at different discharge pressures of thin films deposited over 30 min at a 30 W RF power.

intense re-sputtering observed at 0.27 Pa becomes directly visible as a complete thin film removal for $|r| < 5$ mm.[31] Increasing the pressure to only 0.4 Pa brings the discharge in an intermediate state with much uniform values for the sheet resistance, thickness, and resistivity but yet a significant re-sputtering rate for $|r| < 10$ mm. At 0.53 and 0.67 Pa, the discharge is in the magnetron sputtering mode with sheet resistance and resistivity profiles correlated with the erosion track on the target surface and significantly higher film thickness for $|r| < 10$ mm (above 350 nm). The sheet resistance and resistivity exhibit, as expected,[31] more than two orders of magnitude differences at 0.67 Pa (see for example between values around $|r| \cong 12$ mm and $r < -20$ mm). For completing the physical characterization, the spatial distributions of the average transmittance (400 to 700 nm) and energy band gap at 0.4 and 0.67 Pa are shown in Fig. 2(d and e), respectively. While the transmittance shows a very shallow correlation with the erosion tracks at 0.67 Pa, there is no noticeable link at 0.4 Pa where the transmittance is more than 5% higher than at 0.67 Pa. However, the band gap (measured from Tauc plot) shows a very clear correlation with the erosion track and significantly higher values (above 3.3 eV) much closer to the theoretical values of AZO at 0.4 Pa. Noticeably, the band gap at 0.67 Pa increases from 3.05 eV at $r = -12$ mm to 3.4 eV at $r = -25$ mm, locations that also correspond to lowest resistivity values (see Fig. 2(c)). It is obvious that such a remarkable evolution within a very narrow pressure range offers a unique opportunity to perform the analytical characterization in order to correlate the plasma role and behavior with the physical and chemical parameters of AZO thin films. For this purpose, the same samples were used to perform time-of-flight secondary ion mass spectrometry (TOF-SIMS) and XPS analyses. To avoid the possible physical interference of the measured points by the two methods, the measurements by each technique were performed 1.5 mm apart with respect to a symmetry line along the 50 mm long sample. Al, Zn and Zn/Al intensity ratios by TOF-SIMS are presented in Fig. 3(a–c), respectively. While the spatial distributions of Al and Zn intensity correlates to some extent with sheet resistance and resistivity values presented in Fig. 2, the correlation of Zn/Al intensity ratio with resistivity values is remarkable. First of all, the central part with high re-sputtering at 0.27 Pa shows a noticeable deficit of Zn (Zn/Al intensity ratio below 0.5) that can be attributed to very different sputtering yields by energetic oxygen ions. For example, the sputtering yield as function of oxygen ion energy is presented in Fig. S1 (ESI†) including the Zn/Al yield ratio.[57] The absolute value of the DC self-bias was below 150 V at all pressures and a fact that limits the negative oxygen ion to below 150 eV. For this energy range, the Zn/Al yield ratio exceeds 6 and consequently supports the assumption of the preferential depletion of Zn by ionic bombardment for $|r| < 5$ mm. Ion energy distribution functions measured during AZO deposition by magnetron sputtering in DC and RF operation modes revealed higher energies for DC than RF, reaching close to 500 eV[26] where the Zn/Al yield ratio is still above 4. Since the yield ratio increases sharply by decreasing the ion energy below 75 eV, it further complicates the possibility to avoid Zn depletion in the deposited AZO films. The highly localized Al-rich region for $|r| < 5$ mm correlates very well with the plume-like plasma discharge mode at 0.27 Pa that have been detected with the dual thermal-electrostatic probe.[33] The Zn/Al intensity ratio reached above 2.4 in Fig. 3(c) for $r < -15$ mm at both 0.53 Pa and 0.67 Pa

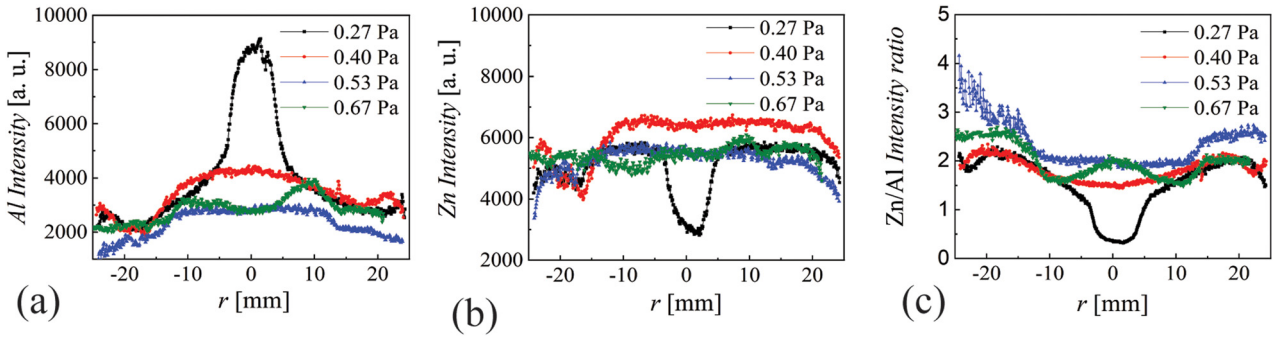

Fig. 3 Spatial distributions of the (a) Al intensity, (b) Zn intensity and (c) Zn/Al intensity ratio measured by TOF-SIMS on the same samples presented in Fig. 2.

where the resistivity was below 10^{-3} Ω cm. The most uniform Zn/Al intensity ratio values, around 2, were obtained for $|r| <$ 15 mm at 0.40 and 0.53 Pa, corresponding to moderate resistivity values around 3×10^{-3} Ω cm. Measuring oxygen by the extremely sensitive TOF-SIMS technique is complicated due to the erroneous contribution of residual gas despite very low operation pressures. In this context, XPS being less sensitive to residual oxygen could give the needed complementary information. The spatial distributions of the O-1s and Zn-$2p_{3/2}$ peaks obtained from XPS at different pressures measured for the same samples presented in Fig. 2 are shown in Fig. 4(a). The Zn depletion for $|r| < 5$ mm is again observed at 0.27 Pa and corresponds to a noticeably high contribution in the O-1s peak at the same location. The same pressures (0.53 and 0.67 Pa) exhibited higher O-1s and lower Zn-$2p_{3/2}$ for $z < -25$ mm where the lower resistivity values have been measured. The Zn/Al ratios at all four pressures are shown in Fig. 4(b) and reveal a very strong Zn depletion for $|r| < 5$ mm, corresponding to the intense and preferential Zn re-sputtering at 0.27 Pa when the discharge is operating in the plume mode, in a very good correlation with TOF-SIMS measurements at 0.27 Pa presented in Fig. 3. However, while the Zn/Al intensity ratio measured by the very sensitive TOF-SIMS method correlates very well with the resistivity profile at all pressures, and the corresponding less sensitive XPS obtained ratios were very noisy at pressures above 0.28 Pa, with no detectable correlation with resistivity. The O_{1s} peak shape suggests that it is composed of ZnO and $Zn(OH)_2$ contributions as presented in Fig. 4(c). The spatial distribution of the ZnO/$Zn(OH)_2$ ratio at different pressures is presented in Fig. 4(d) and shows a pronounced decrease to below 1.5 for $r < -17$ mm where the lowest resistivity values were measured (see Fig. 2(c)). Due to the very low level of Al doping (only 2%), the Al^{+3} peak at 78 eV exhibited a low

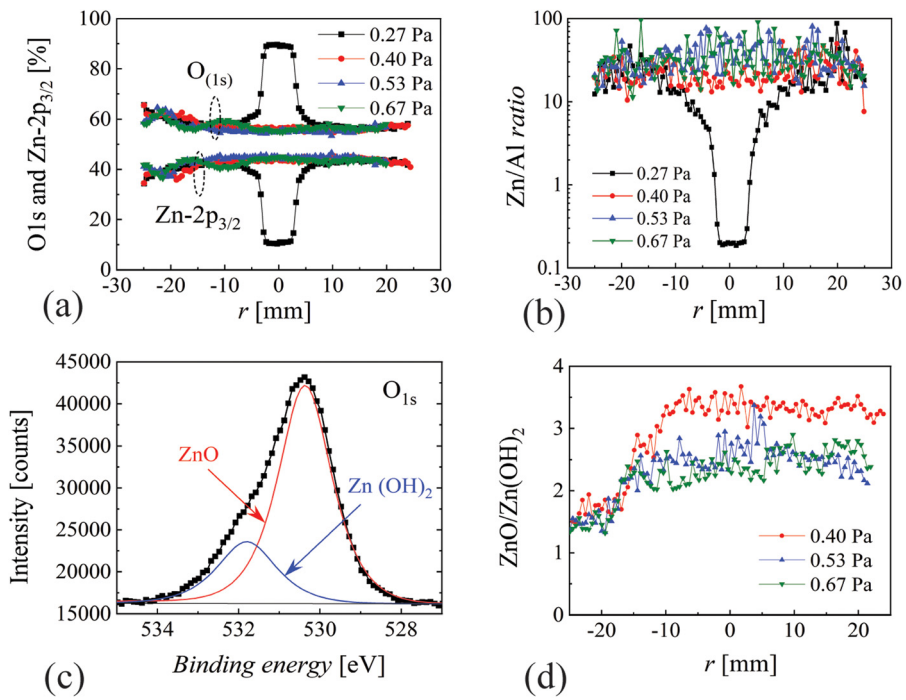

Fig. 4 XPS investigation at different pressures presenting: (a) spatial distributions of O-1s and Zn-$2p_{3/2}$ peaks, (b) the spatial distribution of the Zn/Al ratio, (c) O-1s deconvolution accounting for ZnO and $Zn(OH)_2$ contributions, and (d) the spatial distribution of the ZnO/$Zn(OH)_2$ ratio.

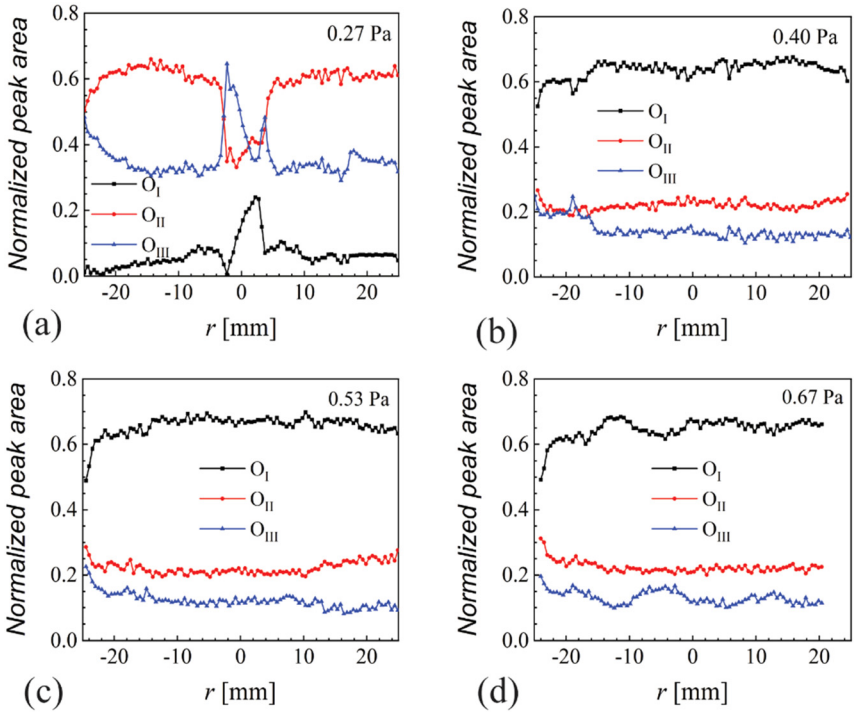

Fig. 5 Spatial distributions of the O-1s deconvolution in O_I, O_{II} and O_{III} contributions at (a) 0.27 Pa, (b) 0.40 Pa, (c) = 0.53 Pa and (d) 0.67 Pa, respectively.

but a detectable intensity. A common way to analyze O-1s was to deconvolute it in three components: 530.15 ± 0.15 eV (O_I) related to the amount of oxygen atoms in a fully oxidized stoichiometric surrounding, 531.25 ± 0.25 eV (O_{II}) related to variations in the

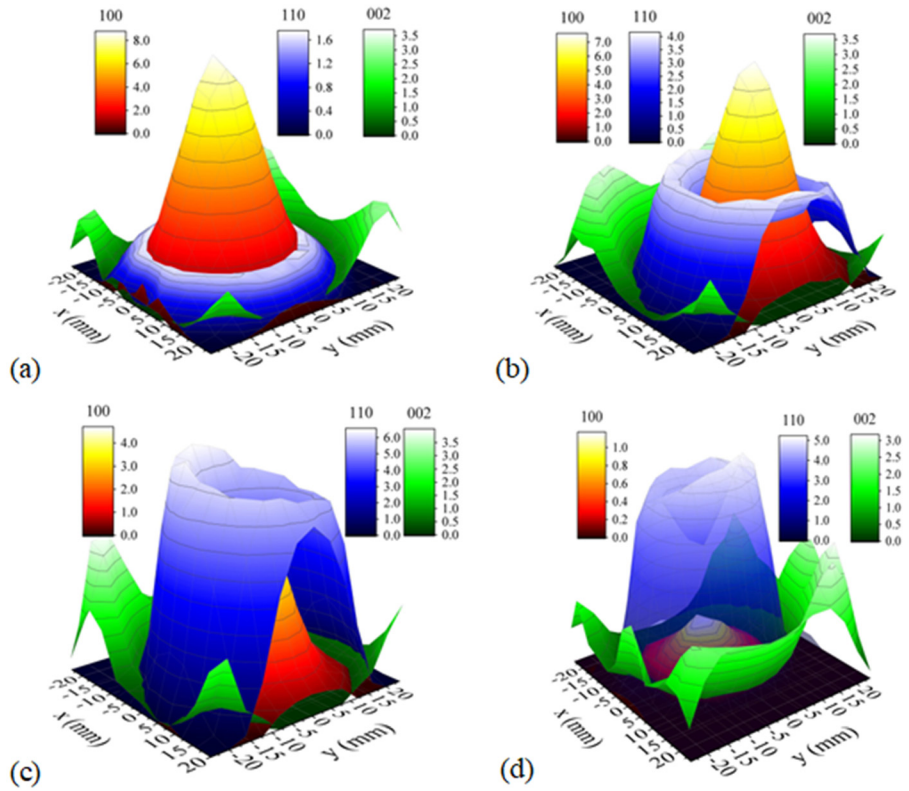

Fig. 6 2D-XRD patterns for (100), (110) and (002) orientations at (a) 0.33, (b) 0.40, (c) 0.47 and (d) 0.53 Pa, respectively.

concentration of oxygen vacancies, and 532.40 ± 0.15 eV (O_{III}) related to loosely bound oxygen on the surface as presented in Fig. 5 at different pressures. Except for the noticeable localized variation for $|r| < 5$ mm at 0.27 Pa, linked to the plume-like plasma, there is no obvious correlation with spatial profiles presented in Fig. 2 except for higher values of O_{III} at the expense of O_I for $r < -25$ mm at 0.53 and 0.67 Pa where the lowest resistivity values were measured. In order to take advantage of the full 2D capability of XRD, pairs of 10 × 50 and 50 × 50 mm^2 soda lime glass samples were deposited at 0.33, 0.40, 0.47 and 0.53 Pa. The 10 × 50 mm^2 samples were used to measure the sheath resistance while the large samples of 50 × 50 mm^2 were used to record the 2D XRD spectra. The sheet resistance values are presented in Fig. S2 (ESI†) and show, despite the very narrow pressure range, a pronounced variation for $|r| < 10$ mm related to the transition from a plume discharge to a magnetron discharge, also connected with intense re-sputtering at lower pressures (0.33 and 0.40 Pa). It is important to specify that the samples at 0.40 and 0.53 Pa are deposited under identical conditions compared to those presented in Fig. 2(a). The 2D mapping on the four 50 × 50 mm^2 samples of (100), (110), and (002) peaks is shown in Fig. 6(a–d), respectively. The correlation of the different zones of the discharge (central, erosion track and edge) with the (100), (110) and (200) peaks, respectively, is remarkable. Moreover, the XRD results correlate very well with the corresponding resistivity values and the Zn/Al intensity ratios obtained by TOF-SIMS. Low resistivity AZO requires the promotion of the *c*-plane (002) Wurtzite orientation while the *m*-plane (110) orientation is desired for applications requiring the anisotropic electrical and mechanical properties such as signal processing and sensors.[58] In an attempt to control the texture orientation, Takayanagi *et al.*[59] used the energetic negative oxygen ions to promote the (110) orientation and the best results were achieved at regions that correlated with the erosion track, which is in very good correlation with the results presented in Fig. 6. The central part of the samples, dominated by the (100) orientation, is strongly correlated with Zn depletion by preferential sputtering as presented in Fig. 3(c). The very narrow range of pressure exhibiting the sharp transition from a dominant (100) orientation at 0.33 Pa to (110) at 0.53 Pa can only be explained by the observed transition from the plume-like discharge to the magnetron discharge, where the main plasma parameters, such as the plasma potential, electron temperature, and plasma density, presents a clear transition that strongly correlates with the self-bias variation included in Fig. 1(c).[33]

4. Conclusion

The properties of AZO thin films have been investigated in a very narrow range of pressures (0.27 to 0.67 Pa) corresponding to the minimum values of the DC self-bias that controls the energy of negative oxygen ions assisting the film growth and providing the lowest resistivity values over a substrate comparable in size with the sputtering target. The TOF-SIMS acquired spatial distribution of the individual Al and Zn intensities was found to correlate to some extent with the sheet resistance and resistivity. However, the Zn/Al intensity ratio was found to correlate extremely well with the resistivity values. This was attributed to the central part having a higher degree of re-sputtering at 0.27 and 0.40 Pa, which is evident from a noticeable deficit of Zn, attributed to a very different sputtering yield by energetic oxygen ions with respect to Al. No obvious correlation was found between the high-resolution XPS spectra (Zn-$2p_{3/2}$ and O-1s) and the sheet resistance and resistivity, except for higher values of loosely bound oxygen on the surface at the expense of the oxygen atoms in fully oxidized stoichiometric surroundings ($r < -25$ mm at 0.53 and 0.67 Pa) where the lowest resistivity values were observed. Moreover, the deconvolution of the O-1s peak in three components revealed a noticeable variation only at the sample center at 0.27 Pa, with very flat profiles at higher pressures, a fact that will need further consideration. The Zn/Al ratio by XPS revealed a significant Zn depletion only for $-10 < r < 10$ mm at 0.27 Pa. At the same time, no detectable correlation could be observed with the same ratio by neither TOF-SIMS nor the resistivity profiles. In contrast, 2D XRD profiles exhibited an excellent correlation with the sheet resistance, resistivity and Zn/Al ratio by TOF-SIMS, resembling the main regions describing the magnetron plasma discharge, respectively: (i) the central part, dominant at low pressures (plume-like discharge) and associated with 100 orientation, (ii) the erosion-track-mirroring, associated with the 110 orientation and the magnetron discharge, which accentuates with the discharge pressure increase, and finally, (iii) the edge or shadow region, associated with the 002 orientation, where the lowest resistivity values are typically reported for very small sample areas with respect to the sputtering target. Since the highest Zn/Al ratios (above 2.5) by TOF-SIMS correlate with the lowest resistivity values and the dominant 002 orientation, it is reasonable to conclude that the high depletion of Zn (Zn/Al < 1.5) observed at the sample center for 0.27 favors the 100 orientation and the mild depletion (Zn/Al < 2.5) associated with the erosion track favors the 110 orientation. So far, special attention was devoted to find an appropriate level of Al doping. However, the present work presents evidence that Zn depletion needs to be compensated or avoided. This aspect points at the need to develop improved physical deposition methods for uniform and low resistivity AZO thin film deposition that could avoid or compensate the intrinsic particularities of the magnetron sputtering discharge.

Author contributions

E. S. designed and directed the research; K. N. performed the TOF-SIMS and XPS characterization and P. N. performed the XRD characterization; E.S. performed the additional experiments and wrote the manuscript, which was discussed and amended by K. N. and P. N.

Conflicts of interest

The authors declare no conflicts of interest.

Acknowledgements

This work was partially supported by the SmartCoating project 6151-00011B, financed by the Innovation Fund Denmark.

References

1 K. Ellmer, *Nat. Photonics*, 2012, **6**, 809–817.
2 C. G. Granqvist, *Sol. Energy Mater. Sol. Cells*, 2007, **91**, 1529–1598.
3 T. Minami, *Semicond. Sci. Technol.*, 2005, **20**, S35–S44.
4 M. B. Cortie, M. D. Arnold and V. J. Keast, *Adv. Mater.*, 2020, **32**, 1–8.
5 S. Seo, S. Jeong, C. Bae, N. G. Park and H. Shin, *Adv. Mater.*, 2018, **30**, 1–8.
6 K. Hagedorn, W. Li, Q. Liang, S. Dilger, M. Noebels, M. R. Wagner, J. S. Reparaz, A. Dollinger, J. Schmedt Auf Der Günne, T. Dekorsy, L. Schmidt-Mende and S. Polarz, *Adv. Funct. Mater.*, 2016, **26**, 3424–3437.
7 M. Gaceur, S. Ben Dkhil, D. Duché, F. Bencheikh, J. J. Simon, L. Escoubas, M. Mansour, A. Guerrero, G. Garcia-Belmonte, X. Liu, M. Fahlman, W. Dachraoui, A. K. Diallo, C. Videlot-Ackermann, O. Margeat and J. Ackermann, *Adv. Funct. Mater.*, 2016, **26**, 243–253.
8 T. Minami, H. Nanto and S. Takata, *Appl. Phys. Lett.*, 1982, **41**, 958–960.
9 K. Ellmer, *J. Phys. D: Appl. Phys.*, 2000, **33**, R17–R32.
10 Z. Ghorannevis, E. Akbarnejad, A. Salar Elahi and M. Ghoranneviss, *J. Cryst. Growth*, 2016, **447**, 62–66.
11 K. H. Patel and S. K. Rawal, *Thin Solid Films*, 2016, **620**, 182–187.
12 C. Zubizarreta, E. G-Berasategui, I. Ciarsolo, J. Barriga, D. Gaspar, R. Martins and E. Fortunato, *Appl. Surf. Sci.*, 2016, **380**, 218–222.
13 A. Sreedhar, J. H. Kwon, J. Yi and J. S. Gwag, *Ceram. Int.*, 2016, **42**, 14456–14462.
14 M. Mickan, U. Helmersson, H. Rinnert, J. Ghanbaja, D. Muller and D. Horwat, *Sol. Energy Mater. Sol. Cells*, 2016, **157**, 742–749.
15 B. Zhao, L. dan Tang, B. Wang, B. wu Liu and J. Heng Feng, *J. Mater. Sci.: Mater. Electron.*, 2016, **27**, 10320–10324.
16 V. Devi, M. Kumar, D. K. Shukla, R. J. Choudhary, D. M. Phase, R. Kumar and B. C. Joshi, *Superlattices Microstruct.*, 2015, **83**, 431–438.
17 J. Nomoto, H. Makino and T. Yamamoto, *J. Appl. Phys.*, 2015, **117**, 045304.
18 F. Fumagalli, J. Martí-Rujas and F. Di Fonzo, *Thin Solid Films*, 2014, **569**, 44–51.
19 N. Evcimen Duygulu, A. O. Kodolbas and A. Ekerim, *J. Cryst. Growth*, 2014, **394**, 116–125.
20 L. Wen, B. B. Sahu, H. R. Kim and J. G. Han, *Appl. Surf. Sci.*, 2019, **473**, 649–656.
21 B. B. Sahu, J. G. Han, M. Hori and K. Takeda, *J. Appl. Phys.*, 2015, **117**, 023301.
22 J. T. Gudmundsson, *Plasma Sources Sci. Technol.*, 2020, **29**, 113001.
23 T. Ishijima, K. Goto, N. Ohshima, K. Kinoshita and H. Toyoda, *Jpn. J. Appl. Phys.*, 2009, **48**, 116004.
24 P. Pokorný, M. Mišina, J. Bulíř, J. Lančok, P. Fitl, J. Musil and M. Novotný, *Plasma Process. Polym.*, 2011, **8**, 459–464.
25 S. Scribbins, M. Bowes and J. W. Bradley, *J. Phys. D: Appl. Phys.*, 2013, **46**, 045203, DOI: 10.1088/0022-3727/46/4/045203.
26 A. Bikowski, T. Welzel and K. Ellmer, *Appl. Phys. Lett.*, 2013, **102**, 10–14.
27 J. Y. Tsao, S. Chowdhury, M. A. Hollis, D. Jena, N. M. Johnson, K. A. Jones, R. J. Kaplar, S. Rajan, C. G. Van de Walle, E. Bellotti, C. L. Chua, R. Collazo, M. E. Coltrin, J. A. Cooper, K. R. Evans, S. Graham, T. A. Grotjohn, E. R. Heller, M. Higashiwaki, M. S. Islam, P. W. Juodawlkis, M. A. Khan, A. D. Koehler, J. H. Leach, U. K. Mishra, R. J. Nemanich, R. C. N. Pilawa-Podgurski, J. B. Shealy, Z. Sitar, M. J. Tadjer, A. F. Witulski, M. Wraback and J. A. Simmons, *Adv. Electron. Mater.*, 2018, **4**, 1600501.
28 J. Meyer, S. Hamwi, M. Kröger, W. Kowalsky, T. Riedl and A. Kahn, *Adv. Mater.*, 2012, **24**, 5408–5427.
29 K. Ellmer and T. Welzel, *J. Mater. Res.*, 2012, **27**, 765–779.
30 Y. Sato, K. Ishihara, N. Oka and Y. Shigesato, *J. Vac. Sci. Technol., A*, 2010, **28**, 895–900.
31 E. Stamate, *Nanomaterials*, 2020, **10**, 14.
32 E. Stamate, *Surf. Coatings Technol.*, 2020, **402**, 126306.
33 M.-A. Petrea and E. Stamate, *Plasma Sources Sci. Technol.*, 2021, **30**, 045002.
34 S. Khan and E. Stamate, *Nanomaterials*, 2022, **12**, 1539.
35 C. Charpentier, P. Prod'homme, I. Maurin, M. Chaigneau and C. P. I. Roca, *EPJ Photovoltaics*, 2022, **2**, 25002.
36 L. Wen, B. B. Sahu, H. R. Kim and J. G. Han, *Appl. Surf. Sci.*, 2019, **473**, 649–656.
37 M. Kumar, L. Wen, B. B. Sahu and J. G. Han, *Appl. Phys. Lett.*, 2015, **106**, 1–6.
38 H. Dondapati, K. Santiago and A. K. Pradhan, *J. Appl. Phys.*, 2013, **114**, 143506.
39 C. Lung, M. Toma, M. Pop, D. Marconi and A. Pop, *J. Alloys Compd.*, 2017, **725**, 1238–1243.
40 D. Miao, S. Jiang, H. Zhao, S. Shang and Z. Chen, *J. Alloys Compd.*, 2014, **616**, 26–31.
41 H. Li, L. K. Schirra, J. Shim, H. Cheun, B. Kippelen, O. L. A. Monti and J. L. Bredas, *Chem. Mater.*, 2012, **24**, 3044–3055.
42 M. Chaves, R. Ramos, E. Martins, E. C. Rangel, N. C. Da Cruz, S. F. Durrant and J. R. R. Bortoleto, *Mater. Res.*, 2019, **22**, e20180665.
43 A. Crovetto, T. S. Ottsen, E. Stamate, D. Kjær, J. Schou and O. Hansen, *J. Phys. D: Appl. Phys.*, 2016, **49**, 295101.
44 D. K. Kim and H. B. Kim, *J. Alloys Compd.*, 2011, **509**, 421–425.
45 P. Misra, V. Ganeshan and N. Agrawal, *J. Alloys Compd.*, 2017, **725**, 60–68.
46 T. Prabhakar, L. Dai, L. Zhang, R. Yang, L. Li, T. Guo and Y. Yan, *J. Appl. Phys.*, 2014, **115**, 0–7.
47 H. M. Kim, C. H. Lee, S. Y. Shon and B. H. Kim, *Appl. Surf. Sci.*, 2017, **421**, 18–23.
48 S. H. Jeong and J. H. Boo, *Thin Solid Films*, 2004, **447–448**, 105–110.

49 S. Y. Tsai, Y. M. Lu, J. J. Lu and M. H. Hon, *Surf. Coat. Technol.*, 2006, **200**, 3241–3244.
50 T. Tsuji and M. Hirohashi, *Appl. Surf. Sci.*, 2000, **157**, 47–51.
51 C. P. Liu, Z. H. Li, K. O. Egbo, C. K. Kwok, X. H. Lv, C. Y. Ho, Y. Wang and K. M. Yu, *J. Phys.: Condens. Matter*, 2021, **33**, 465703.
52 R. Cebulla, R. Wendt and K. Ellmer, *J. Appl. Phys.*, 1998, **83**, 1087–1095.
53 B. Szyszka, *Thin Solid Films*, 1999, **351**, 164–169.
54 B. P. Shantheyanda, V. O. Todi, K. B. Sundaram, A. Vijayakumar and I. Oladeji, *J. Vac. Sci. Technol., A*, 2011, **29**, 051514.
55 C. Charpentier, P. Prod'Homme and P. Roca i Cabarrocas, *Thin Solid Films*, 2013, **531**, 424–429.
56 V. Tiron, L. Sirghi and G. Popa, *Thin Solid Films*, 2012, **520**, 4305–4309.
57 N. Matsunami, Y. Yamamura, Y. Itikawa, N. Itoh, Y. Kazumata, S. Miyagawa, K. Morita, R. Shimizu and H. Tawara, *At. Data Nucl. Data Tables*, 1984, **31**, 1–80.
58 W. R. Ali and M. Prasad, *Sens. Actuators, A*, 2020, **301**, 111756.
59 S. Takayanagi, T. Yanagitani and M. Matsukawa, *Appl. Phys. Lett.*, 2012, **101**, 1–4.

